PHYSICAL REVIEW E **89**, 053302 (2014)

Three-dimensional simulation strategy to determine the effects of turbulent mixing on inertial-confinement-fusion capsule performance

Brian M. Haines,* Fernando F. Grinstein, and James R. Fincke
Los Alamos National Laboratory, MS T087, Los Alamos, New Mexico 87545, USA
(Received 17 March 2014; published 8 May 2014)

In this paper, we present and justify an effective strategy for performing three-dimensional (3D) inertial-confinement-fusion (ICF) capsule simulations. We have evaluated a frequently used strategy in which two-dimensional (2D) simulations are rotated to 3D once sufficient relevant 2D flow physics has been captured and fine resolution requirements can be restricted to relatively small regions. This addresses situations typical of ICF capsules which are otherwise prohibitively intensive computationally. We tested this approach for our previously reported fully 3D simulations of laser-driven reshock experiments where we can use the available 3D data as reference. Our studies indicate that simulations that begin as purely 2D lead to significant underprediction of mixing and turbulent kinetic energy production at later time when compared to the fully 3D simulations. If, however, additional suitable nonuniform perturbations are applied at the time of rotation to 3D, we show that one can obtain good agreement with the purely 3D simulation data, as measured by vorticity distributions as well as integrated mixing and turbulent kinetic energy measurements. Next, we present results of simulations of a simple OMEGA-type ICF capsule using the developed strategy. These simulations are in good agreement with available experimental data and suggest that the dominant mechanism for yield degradation in ICF implosions is hydrodynamic instability growth seeded by long-wavelength surface defects. This effect is compounded by drive asymmetries and amplified by repeated shock interactions with an increasingly distorted shell, which results in further yield reduction. Our simulations are performed with and without drive asymmetries in order to compare the importance of these effects to those of surface defects; our simulations indicate that long-wavelength surface defects degrade yield by approximately 60% and short-wavelength drive asymmetry degrades yield by a further 30%.

DOI: 10.1103/PhysRevE.89.053302 PACS number(s): 47.27.ep, 52.57.Fg, 52.35.Ra

I. INTRODUCTION

Inertial confinement fusion (ICF) uses a uniform laser or x-ray drive to heat a spherical shell, which then ablates, generating a reactive force that implodes fuel, typically a mixture of deuterium and tritium, inside the shell. The convergence of the fuel raises its pressure, causing a deceleration of the shell and converting its kinetic energy into internal energy in the fuel and thus initiating fusion reactions [1]. Several phases of the implosion are known to be subject to hydrodynamic instabilities. The interface between the shell and surrounding gas is Rayleigh-Taylor unstable as the shell material ablates. In addition, the interface between the shell and fuel is Richtmyer-Meshkov unstable as a shock generated by the ablasion exits the shell, as well as during subsequent interactions between the shell and reflected shocks. This interface is also Rayleigh-Taylor unstable when the shell decelerates. These turbulent instabilities are seeded by asymmetries in the drive and on the surfaces of material interfaces. Understanding turbulent instability growth and corresponding material mixing during the implosion and burn of ICF capsules is important for determining their performance. Indeed, turbulence development may displace fuel in the hot spot (the hot, dense core of the implosion where a majority of the fusion reactions occur) and cause mixing of cold shell material with the fuel; these effects may degrade capsule yield significantly. Nevertheless, accurate prediction of turbulence development and the amount of material mixing that occurs during an implosion is hindered by our present computational capabilities.

Performing simulations of ICF capsules is a particularly difficult task due to the range of physics and scales involved. Using present computational power, it is necessary to either ignore relevant physics in the problem or reduce the dimensionality in order to successfully complete a simulation of an ICF implosion. It is well known, however, that reduced dimension [one-dimensional (1D) and two-dimensional (2D)] hydrodynamic simulations significantly underpredict the growth of various hydrodynamic instabilities due to the absence of vortex-stretching effects (see, e.g., [2]). An intermediate approach, pioneered by Thomas and Kares in Ref. [3], involves starting the simulation in 2D then rotating it to three dimensions (3D) once sufficient convergence of the ICF capsule has been achieved. Using this approach, Thomas and Kares demonstrate the effects of drive asymmetry on the development of turbulence in the implosion through Bell-Plesset related convergence effects [4], in which perturbations of an incompressible fluid interface grow during an implosion as a consequence of mass conservation. In this paper, we qualify and generalize the use of such an approach in order to study the impact of surface defects and drive asymmetry in promoting the development of turbulent instabilities and associated material mixing, as well as their effects on capsule yield.

In order to address the possible limitations of the use of a 2D-3D rotation strategy, we employ this approach to perform simulations of a laser-driven reshock experiment for which fully 3D simulation data are available [5]. The reshock experiment involves similar physics to that in an ICF implosion but does not involve the convergence (implosion) physics, which makes the problem tractable for performing a fully 3D simulation. We show that, when (nominally) 2D initial conditions are used as in the pure 2D-3D data rotation, the

*bmhaines@lanl.gov

growth of physical 3D modes is significantly inhibited and the simulation does not develop sufficient turbulence nor turbulent mixing to match the fully 3D simulations, despite the presence of grid-scale azimuthal perturbations of the 2D rotated data. In contrast, we find that we can generate turbulence and mixing that satisfactorily compare to that in the fully 3D simulation when additional (azimuthal) perturbations are applied to the 2D-3D mapping function at the time of rotation. These perturbations compensate for the reduced growth of turbulent instabilities during the 2D phase of the simulation as well as the artificial smoothing of the data in the azimuthal direction caused by the 2D-3D rotation.

Reduced-dimension simulations are known to overpredict the yield of ICF capsules compared to experiment (see, e.g., [6–9], among many others). Many explanations have been suggested, for example, turbulent mixing seeded by drive asymmetry [3,10–12], the depletion of high-energy ions due to their long mean free paths [13], and the presence of self-generated electric and magnetic fields that are not typically modeled in simulations [14]. While reduced-dimension simulations can be tuned to achieve reasonable results [10,11,15,16], they do not provide predictive capability. Furthermore, three-dimensional ICF simulations that have been performed [3,17] have not considered or adequately resolved the effects of long-wavelength asymmetries, which have the largest amplitudes [9,11]. In this paper, we use our developed simulation strategy to demonstrate that turbulent instabilities seeded by long-wavelength surface defects and short-wavelength drive asymmetries are sufficient to explain the discrepancies between the yield predicted by previous reduced-dimension simulations of ICF implosions and experiments. Our simulations indicate that this is achieved primarily through the displacement of fuel away from the hot spot by shell material. This provides evidence for a recent hypothesis in Ref. [16], which suggests that long-wavelength asymmetries in the x-ray drive of a National Ignition Facility (NIF) capsule may be a significant source of distorted hot-spot shapes and yield degradation. It also supports the supposition in Ref. [18] that escaping fuel mass may be the cause of discrepancies between the size of the fuel assembly as predicted by 2D simulations and observed experimentally.

The paper proceeds as follows. In Sec. I A, we discuss the simulation strategies employed in both the reshock and ICF simulations. Next, in Sec. II, we review the reshock experiment, discuss the 2D-3D simulation strategy employed to simulate it, and compare the results from this and standard 2D-3D strategies to our previously reported fully 3D simulation data. In Sec. III, we detail application of our new 2D-3D strategy to an OMEGA-type ICF capsule and discuss results, comparing them to available experimental data. Finally, in Sec. IV, we present our conclusions.

A. Simulation strategies

Laboratory observations typically provide only limited integrated measures of complex nonlinear three-dimensional physical processes leaving many details and mechanisms unresolved. Carefully controlled computational experiments based on the numerical simulations play a crucial complementary role, providing insight into the underlying dynamics. Collaborative laboratory and computational studies establish predictability of the models in conjunction with the development of frameworks for analysis, metrics for verification and validation, and uncertainty quantification.

Resolution requirements make direct numerical simulation (DNS) nearly impossible for most practical regimes and geometries even on the largest supercomputers. On the other end of the simulation spectrum are the Reynolds-averaged Navier-Stokes (RANS) approaches, which are the preferred industrial standard; RANS solves the flow equations averaged over an ensemble of realizations and requires closure models. In three-dimensional (3D) coarse grained simulation (CGS) strategies, large energy containing structures are resolved, smaller structures are filtered out, and unresolved sub-grid scale (SGS) effects are modeled; this includes classical large-eddy simulation (LES) strategies [19] with explicit use of SGS models, and implicit LES (ILES) [20], relying on SGS modeling implicitly provided by physics capturing numerical algorithms. The CGS strategy of separating resolved and SGS physics effectively becomes the intermediate approach between DNS and RANS.

Turbulent material mixing can be usefully characterized by the fluid physics involved: large-scale entrainment, stirring due to velocity gradient fluctuations, and molecular diffusion. At moderately high Reynolds number (Re), when convective time scales are much smaller than those associated with molecular diffusion, we are primarily concerned with the numerical simulation of the first two convectively driven processes. These processes can be captured with sufficiently resolved implicit large-eddy simulation (ILES) [20]. Moreover, by combining shock and turbulence emulation capabilities based on a single model, ILES offers a natural effective simulation strategy to capture shock-driven turbulence phenomena in the ICF context. Therefore, ILES serves as our primary simulation strategy.

In Ref. [5], we used an ILES strategy to perform 3D simulations of laser-driven reshock experiments performed at the University of Rochester's OMEGA laser facility [21]. We validated the simulations through direct comparison of simulation and radiographic data, as well as comparisons with theoretical and DNS results on homogeneous isotropic turbulence. Despite the fact that the flow is neither homogeneous, isotropic, nor fully turbulent, there are local regions in which the flow demonstrates characteristics of homogeneous isotropic turbulence, which can be identified and isolated by the presence of high levels of turbulent kinetic energy (TKE) and vorticity. After reshock, our analysis shows characteristics consistent with those of incompressible isotropic turbulence. Self-similarity and effective Reynolds number assessments suggest that the results are reasonably converged at the finest resolution. Our results show that in shock-driven transitional flows, turbulent features such as self-similarity and isotropy only fully develop once decorrelation, characteristic vorticity distributions, and integrated TKE have decayed significantly.

The present simulations were performed using an implicit large-eddy simulation (ILES) strategy [20] based on LANL's radiation adaptive grid Eulerian (RAGE) hydrodynamics code [22]. RAGE solves the Euler form of the multimaterial compressible inviscid conservation equations for mass density

(ρ), momenta ($\rho\vec{u}$), and total specific energy (E), given by

$$\begin{aligned}\frac{\partial\rho}{\partial t}+\nabla\cdot(\rho\vec{u})&=0,\\ \frac{\partial\rho\vec{u}}{\partial t}+\nabla\cdot(\rho\vec{u}\vec{u}+pI)&=0,\\ \frac{\partial\rho E}{\partial t}+\nabla\cdot(\rho\vec{u}E+p\vec{u})&=0,\\ \frac{\partial c_i\rho}{\partial t}+\nabla\cdot(c_i\rho\vec{u})&=0,\end{aligned}\tag{1}$$

where $i=l,2,\ldots,M$, M is the number of material species, ρ is the mass density, c_i is the mass fraction of the ith species, $\vec{u}$ is the fluid velocity, and p is the pressure. The hydrodynamic equations are supplemented with SESAME tabular equations of state [23]. Radiation transport is neglected in the reshock problem, as the ratio of typical radiative to hydrodynamic fluxes can be estimated as $\sigma T^4/(\rho U^3)\approx 10^{-4}$, where σ is the Stefan-Boltzmann constant and $T=10$ eV, $U=80$ km/s, and $\rho=0.2$ g/cc are characteristic of the experiment. For the ICF problem, single group radiation diffusion is used along with a three-temperature (ion, electron, and radiation) treatment as well as electron and ion heat conduction.

RAGE uses a second-order Godunov finite volume scheme, adaptive mesh refinement (AMR) using cubic cells, as well as a variety of numerical options. In the present simulations, we use a Van Leer limiter, no material interface treatment, and as in our recent work [2] a particular artificial diffusion option meant to compensate for anisotropic errors due to directional splitting was not activated. As used in this work (based on nominally inviscid equations), RAGE models miscible material interfaces and high Reynolds number convection-driven flow with an effective (numerical) viscosity determined by the small-scale cutoff and residual numerical diffusion of the simulation algorithm. Details of the 2D-3D simulation procedure varied between the reshock and ICF problems due to the differing geometries of the problems, and are provided in the relevant sections below. The ILES simulation strategy as implemented in RAGE has been used extensively to model relevant high energy density physics experiments and has been validated in this context through both code comparison work [24], involving codes with a variety of simulation strategies, and direct comparison to experiment [5,25,26].

For the ICF simulations, the new Singe package in RAGE was used to simulate thermonuclear reactions. This package tracks material isotopes and calculates thermonuclear reaction rates. In each computational cell, these obey the formula $f=\frac{n_1 n_2\langle\sigma v\rangle}{V_{\rm eff}}$, where f is the reaction rate, n_i is the number of reactants of the ith species, v is the relative velocity of two reactants, $\langle\ldots\rangle$ indicates averaging over an effective velocity distribution σ as a function of $T_{\rm ion}$, and $V_{\rm eff}$ is the effective volume. The value of f is halved for reactions involving a species of nuclei reacting with itself. The effective volume $V_{\rm eff}$ can be calculated in two limits to obtain bounds on the reaction rate: a "clean" limit and a fully atomically mixed limit. In the former limit, $V_{\rm eff}$ is set to be the volume of the reactants in each cell. In the atomically mixed limit, $V_{\rm eff}$ is set to the volume of the computational cell. The true burn rate lies somewhere between these limits and varies between cells; we present these limits in the absence of any information about the distribution of materials at a sub-grid scale level. Singe assumes that all charged particle reaction products are deposited locally and that neutrons are lost from the system.

ICF simulations were performed at three different maximum resolutions: 1/2, 1/4, and 1/8 μm. The 1/2- and 1/4-μm simulations were run on LANL's Cielo supercomputer, employing a maximum of 1.1 billion and 6.4 billion cells, respectively, and a total of 0.01 and 0.2 Cielo days. The number of processors used was varied as the simulations progressed; the 1/2-μm simulations used a maximum of 4096 processors and the 1/4-μm simulations used a maximum of 16 384 processors. The 1/8-μm simulation was run in the 2D phase on Cielo, using 0.14 Cielo days, then completed in 3D on LLNL's Sequoia supercomputer, using a further 1.1 Sequoia days with as many as 131 072 processors and a maximum of 36 billion cells.

II. TESTING AND VALIDATING THE 2D-3D STRATEGY: RESHOCK EXPERIMENT

A. Description of the experiment

The experiments, outlined in detail in Ref. [21], were performed using the University of Rochester's OMEGA laser. The target consists of a cylindrical beryllium (Be) tube $\approx$1.4 mm in length and $\approx$0.5 mm in diameter with a $\approx$100-μm wall thickness (see Fig. 1). The target is successively hit from both sides by two laser-driven shocks. The first, $\approx$5 kJ, at $t=0$ ns impacts the plastic ablator on the left, driving a Mach $\approx$5 shock through the 20-μm aluminum tracer disk adjoining the ablator. The tracer disk is thus propelled to the right down the center of the cylinder, which is filled with a low-density (60 mg/cc) CH foam. The second shock, $\approx$4 kJ at 5 ns, impacts a plastic ablator at the right end of the tube. The shocks collide at approximately 8 ns to the right of the mixing layer and the second shock hits (reshocks) the mixing layer at approximately 10 ns, causing it to compress until approximately 13 ns.

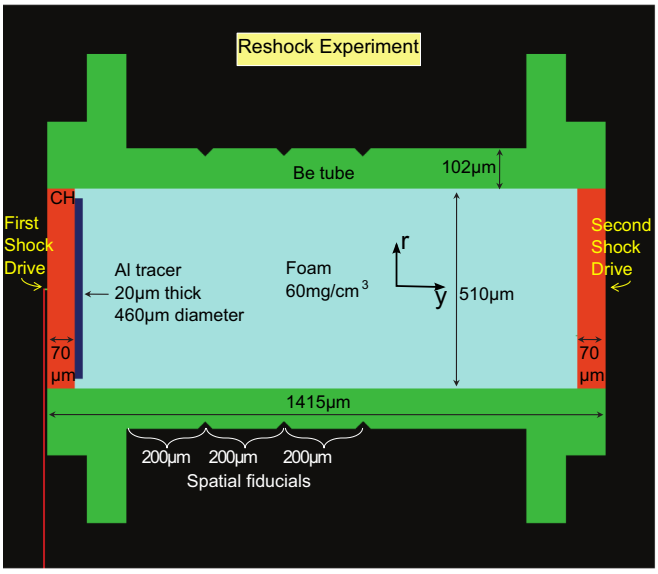

FIG. 1. (Color online) Target geometry.

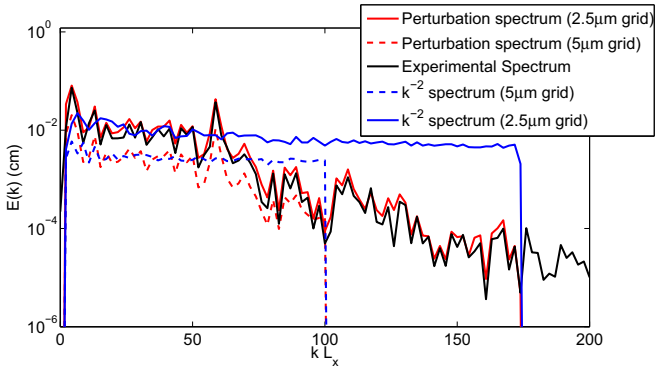

FIG. 2. (Color online) Spectra of interface perturbations. Here, $L_x = 460$ μm, the initial width of the aluminum tracer.

At approximately 17 ns, the second shock exits the mixing layer. At later times (beyond the present scope), the mixing layer is further affected by compression and expansion waves and secondary shocks generated by reflections at the Be tube interface.

B. Initial material interface conditions

As we consider simulating the Richtmyer-Meshkov instability (RMI) in laboratory experiments, we must consider the effects of modeling initial conditions (ICs), for which limited experimental characterizations are available. The difficulties with the open problem of predictability of material stirring and mixing by under-resolved multiscale turbulent velocity fields in shock-driven turbulent flows are compounded with the inherent sensitivity of turbulent flows to ICs [27,28]. Flow instabilities driven by accelerated material interfaces are particularly sensitive to their ICs: small variations in the initial state of the interface can result in significant changes to the integral character of a mixing layer at late times [29–31].

The aluminum interfaces were perturbed using deformations with spectral content, shown in Fig. 2, emulating as closely as possible that measured from the samples in the laboratory experiments. Specifically, for 3D simulations, the aluminum surfaces parallel to the shock front were perturbed using the function

$$\zeta(x,z) = \chi\Gamma \sum_{i,j=0}^{N} c_{ij} \cos\left(\frac{2\pi i x}{l_x} + \theta_i\right) \cos\left(\frac{2\pi j z}{l_z} + \phi_j\right), \tag{2}$$

where $\theta_i, \phi_j \in [0, 2\pi]$ and $c_{ij} \in [0,1]$ were chosen randomly using a uniform distribution and weighted appropriately to achieve the desired spectrum and x and z denote orthogonal directions along the surface of the tracer. N was set so that the spectrum was cut off at $\lambda = 2.5$ μm, the size of the smallest cell in the high resolution run. Γ was set in order that the perturbations have a standard deviation of 0.33 μm over the 2.5-μm 3D grid, corresponding to that of the laboratory data. For the 3D simulation, $\chi = 1$. For the 2D-3D simulations, the surface of the aluminum tracer was perturbed at $t = 0$ using the function $\zeta(x,0)$, and χ was varied to enhance the interface perturbations, as discussed in the following.

C. 2D-3D mapping and flow initialization strategies

In all cases we performed the 2D-3D mapping at 10 ns, immediately before reshock. First, we examined the impact of changing the surface roughness amount specified by the function $\zeta(x,z)$ defined in Eq. (2) and parametrized in terms of χ, in the context of the unperturbed mapping, i.e., pure data rotation, in which all state and velocity variables were set using the mapping

$$\begin{Bmatrix} x \\ y \end{Bmatrix} = \begin{Bmatrix} \sqrt{x'^2 + z'^2} \\ y' \end{Bmatrix},$$

where (x,y) are the coordinates for the 2D problem and (x',y',z') are the coordinates for the 3D problem. Vector-valued quantities, such as the velocity, were also appropriately rotated. Next, we also considered simulations where the 2D-3D mapping itself was modified using the perturbation function $\zeta(x,z)$ defined in Eq. (2) and parametrized in terms of χ. Specifically, the perturbed mapping was defined as

$$\begin{Bmatrix} x \\ y \end{Bmatrix} = \begin{Bmatrix} \sqrt{x'^2 + z'^2} \\ y' + \zeta(x',z') \end{Bmatrix}.$$

D. Hydrodynamic instability growth in the reshock experiment

Turbulence generation in the reshock experiment is associated primarily with the Richtmyer-Meshkov instability (RMI). Richtmyer [32] derived an expression for the growth of a perturbation subject to an incident shock wave:

$$\frac{da}{dt} = kAa_0u_c, \tag{3}$$

where k is the wave number, $A = \frac{\rho_0 - \rho_1}{\rho_0 + \rho_1}$ is the post-shock Atwood number, $a_0 = \frac{1}{2}(a_{0-} + a_{0+})$ is the initial amplitude (a_{0-} is preshock and a_{0+} is post shock), and u_c is the change in interface velocity due to the shock. Using values appropriate to the reshock experiment ($k = 4\pi/460$ μm corresponding to the longest wavelength IC perturbation, $A \approx 0.97$ and $u_c \approx 10^7$ cm/s), we can obtain an estimate of $a(10\text{ ns})/a_0 \approx 30$, which provides a rough estimate of the growth factor of the interface perturbations at the time of 2D-3D rotation. Formula (3) is valid in the linear growth regime for RMI, in particular, experimental and numerical comparisons in [33] suggest it is valid for $ka_0 < 1$. For the values used above, we have $ka_0 \approx 0.007$.

The above analysis considers the growth of only the longest-wavelength perturbation. It is likely that since the longer wavelengths have the largest amplitude (see Fig. 2), these dominate the hydrodynamic development of the experiment, so it is most important to capture their growth correctly. Nevertheless, our initial perturbation spectra includes a wide range of modes, many of which are outside of the linear regime $ka_0 < 1$. As a further complication, the growth of these modes is, in reality, coupled. A rationale for justifying the relevance of this estimate comes from our recent RMI simulation work Ref. [34–36] (see, e.g., Fig. 9 in Ref. [34] and Fig. 5 in Ref. [36]). Shock-driven flows are typically investigated using the early-time relevant RMI model for a first-shocked relatively flat and thin material interface modeled by Richtmyer formula above [32]. However, for most classes

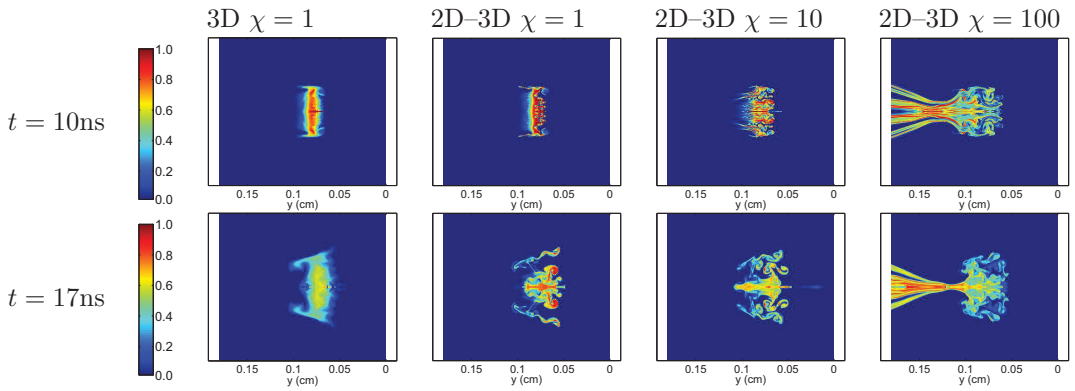

FIG. 3. (Color online) c_{Al} plots for simulations of the reshock experiment; here, 2D-3D perturbations are applied in 2D at $t = 0$.

of shock-induced mixing, reshocks which happen at a later time and involve morphologically more complex interfacial layers and fluid instability mechanisms distinctly different from the classical RMI are more important phenomena [36]. Before reshock, growth tends to follow Richtmyer's formula: shorter wavelengths grow faster, whereas after reshock actual growth features get inverted and the dominant modes are the longer wavelengths reflecting what we have called the bipolar behavior of the RMI [35].

E. Augmenting initial perturbation level in 2D-3D pure-rotation context

In this section, we will show results from performing 2D-3D simulations where the initial 2D surface perturbations are augmented by a factor χ. We will demonstrate that this method does not produce satisfactory results in comparison to purely 3D simulation data. Therefore, this method *will not* be used subsequently for ICF simulations. However, we present these results for completeness and as a caveat to others who may want to try it.

In Fig. 3, we show 2D plots of the aluminum concentrations c_{Al} for the 2D-3D simulations (azimuthally averaged for $t \geqslant 10$ ns) compared to azimuthally averaged values for the purely 3D simulation. The magnitude of the initial interface perturbations was kept fixed [$\chi = 1$ in Eq. (2)] for the 3D simulation and varied for the 2D-3D simulations ($\chi = 1, 10, 100$). Note that in the $\chi = 100$ case (experimentally observed perturbations enhanced by a factor of 100), the aluminum tracer is fragmented from the perturbations at $t = 0$. In all of the 2D-3D cases presented here, the aluminum is significantly more concentrated and fragmented than in the 3D case, and no satisfactory comparison is obtained.

In Fig. 4, we show a volumetrically integrated measure of the density-weighted velocity variance, turbulent kinetic energy TKE, as a function of time. We define the local velocity variance TKE as

$$K(y,r) := \frac{\left\langle \frac{1}{2}\rho((u_r - \tilde{u}_r)^2 + (u_y - \tilde{u}_y)^2 + u_\theta^2)\right\rangle_\theta}{\langle \rho \rangle_\theta}, \quad (4)$$

where $\langle \ldots \rangle_\theta$ denotes azimuthal averaging and $\tilde{u}_i := \langle u_i \rho \rangle_\theta / \langle \rho \rangle_\theta$. The 2D-3D simulations presented all significantly underpredict the integrated TKE when compared to the purely 3D simulation.

In Fig. 4, we also show an integrated mixing measure as a function of time, defined by

$$\text{mixing} := \int_V \rho^2 c_{\mathrm{Al}} c_{\mathrm{foam}} dV, \quad (5)$$

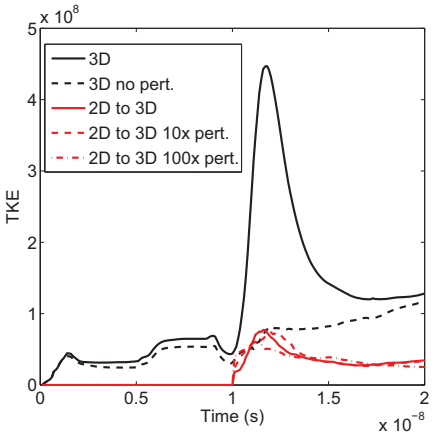

Comparison of integrated TKE

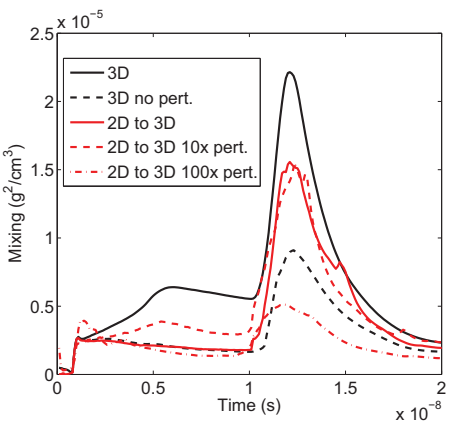

Comparison of integrated mixing

FIG. 4. (Color online) Integrated flow quantities for the reshock simulations; here, 2D-3D perturbations are applied in 2D at $t = 0$.

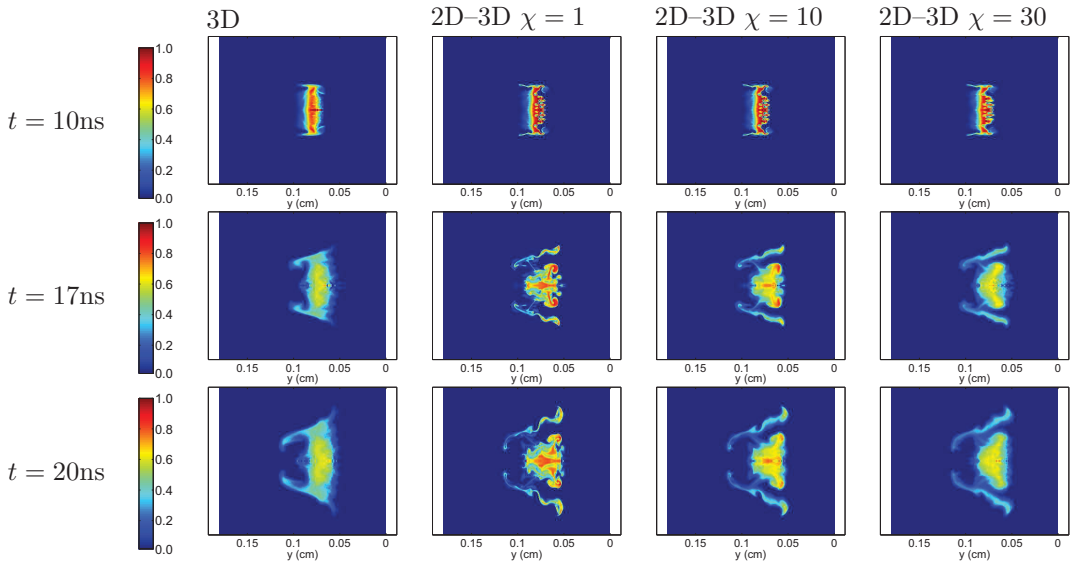

FIG. 5. (Color online) c_{Al} plots; here, 2D-3D perturbations are applied in 3D at the time of rotation at $t = 10$ ns.

where azimuthally averaged fields are used when the data is 3D and the integration is performed over the entire 2D computational domain (thus allowing us to compare the results even when the 2D-3D data have not yet been rotated to 3D). The 2D-3D simulations all significantly underpredict the amount of mixing when compared to the 3D data.

By all metrics considered, the 2D-3D simulation strategy is insufficient to obtain reasonable comparisons to 3D simulation data when augmenting initial perturbation level of 2D ICs in 2D-3D pure-rotation context. This is likely due to the fact that increased turbulence generation during the 2D phase of the simulation is offset by the artificial azimuthal smoothing of the 2D-3D rotation procedure.

F. Generalized 2D-3D mapping with perturbations

In this section, we show results for 2D-3D simulations where the 2D-3D mapping is additionally perturbed (azimuthally) based on the initial surface roughness. We will show that this method produces satisfactory results compared to purely 3D simulation data when the mapping perturbations are set at a factor of $\chi = 30$ times the initial surface roughness level. This corresponds to the approximate RMI growth rate of the longest-wavelength mode between $t = 0$ and 10 ns, the time at which the simulation is rotated to 3D.

In Fig. 5, we show 2D plots of the aluminum concentrations c_{Al} for the 2D-3D simulations (azimuthally averaged for $t \geqslant 10$ ns) compared to azimuthally averaged values for the purely 3D simulation. In all cases, the initial aluminum tracer interfaces were perturbed using experimental data (i.e., $\chi = 1$). In addition, for the 2D-3D data, the state and velocity variables were perturbed upon rotating the data to 3D at $t = 10$ ns, using the method outlined in Sec. II C with $\chi = 1, 10, 30$. A satisfactory comparison is obtained for the case $\chi = 30$, corresponding to the long-wavelength RMI growth

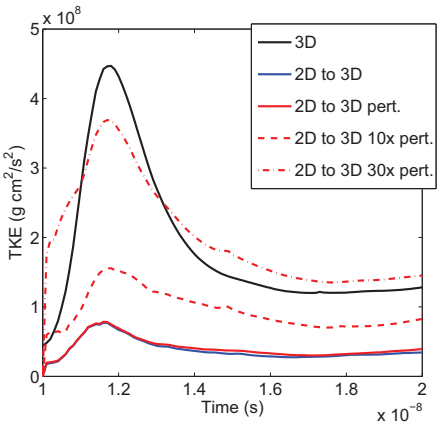

Comparison of integrated TKE

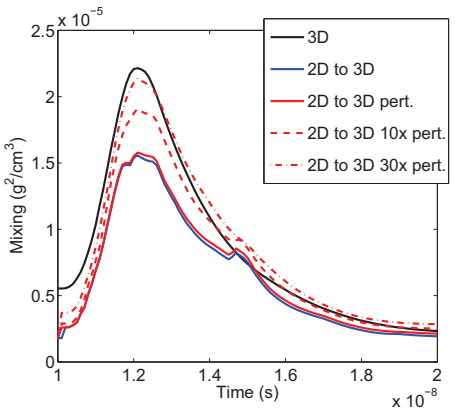

Comparison of integrated mixing

FIG. 6. (Color online) Integrated flow quantities for the reshock simulations; here, 2D-3D perturbations are applied in 3D at the time of rotation at $t = 10$ ns.

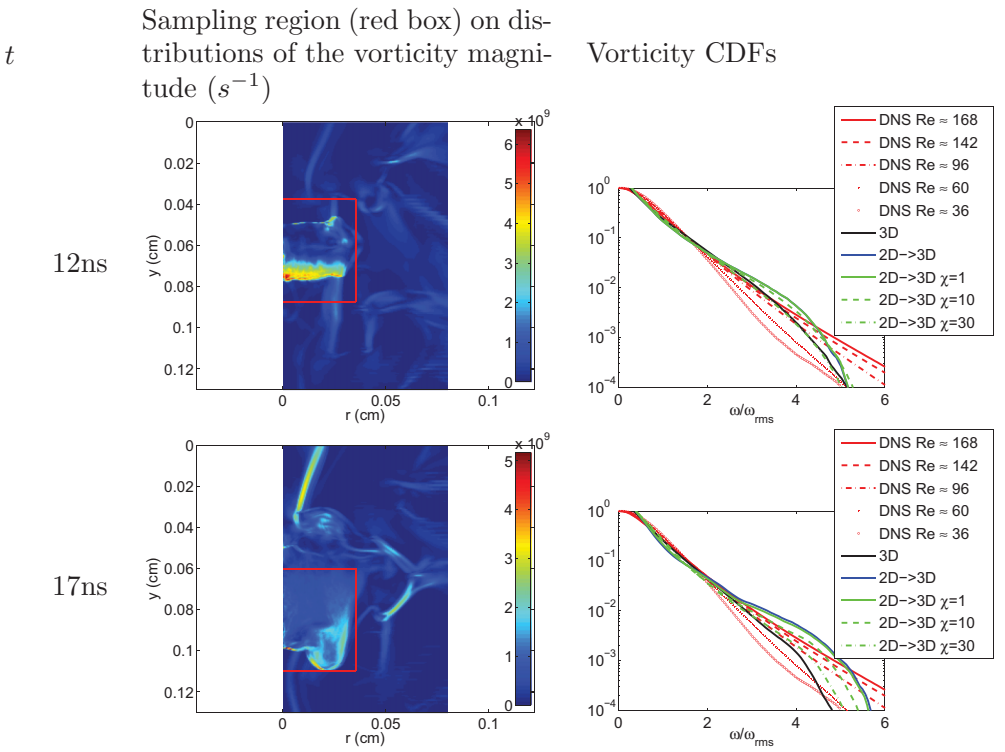

FIG. 7. (Color online) CDFs of vorticity $\omega/\omega_{\mathrm{RMS}}$ sampled from a uniform 5-μm grid. Sampling regions (within red lines) on distributions of vorticity magnitude (s^{-1}). The DNS data were taken from [37].

rate up to the time of rotation. For the cases $\chi = 1,10$, the aluminum concentration is significantly fragmented and overly concentrated compared to the 3D data.

In Fig. 6, we show a comparison of a density-weighted volumetrically integrated measure of the velocity variance, defined in Eq. (4). The peak TKE value increases nonlinearly with the magnitude of the interface perturbations (χ). For the case $\chi = 30$, a reasonable comparison is obtained with the 3D data. In Fig. 6, we also show a comparison of an integrated mixing measure defined in Eq. (5). The peak mixing value increases nonlinearly with the magnitude of the interface perturbations (χ). For the case $\chi = 30$, a good comparison is obtained with the purely 3D data.

In Fig. 7, we show CDFs of the vorticity magnitude $\omega/\omega_{\mathrm{RMS}}$, where ω_{RMS} is the root mean square vorticity, for 2D-3D simulations and compare them to those corresponding to DNS of isotropic turbulence data from Jiménez *et al.* [37] and our purely 3D simulations [5]. CDF(ω), the integral of PDF(ω), represents the volume fraction with vorticity magnitude greater than ω. The CDFs associated with the DNS data tend to approach a high Re_λ limit when Re_λ is above the mixing transition threshold $\mathrm{Re}_\lambda \approx 100$–$140$ [39,40], where Re_λ is based on the Taylor microscale λ. Of the 2D-3D simulation data, the case with $\chi = 30$ compares best with the purely 3D data, with almost negligible differences at $t = 12$ ns. The quality of the comparison degrades only slightly by $t = 17$ ns.

By all measures considered, a good comparison can be obtained with purely 3D data by performing a 2D-3D simulation where the 2D-3D mapping is perturbed using the experimentally observed initial condition perturbations enhanced by a factor of $\chi = 30$, corresponding to the RMI growth rate of the longest-wavelength mode up to the time of rotation.

G. Effects of simulating a quadrant of the reshock problem

Here, we assess the possible effects of simulating only a quadrant of the reshock problem, which is a reasonable approximation given the rotational symmetry of the problem. Nevertheless, this can introduce inaccuracies due to the fact that there are differently allowed azimuthal constraints and nonlinear mode couplings when only a single quadrant of the reshock problem is involved. In order to assess the possible limitation effects of simulating a quadrant of the problem, we performed both single-quadrant and full 3D simulations at 2.5 μm and compared the results.

In Fig. 8, we show plots of the integrated TKE and mixing, respectively, for both the full 3D and 3D single-quadrant simulations. The differences are minor but noticeable. For the quadrant simulation, the TKE peak is delayed and the mixing peak diminished slightly. Moreover, TKE peak values (and hence TKE production mechanisms) are found to be well resolved at this 2.5-μm resolution [38].

H. Summary of results for the reshock problem

We considered two methods of perturbing 2D-3D simulation data in order to enhance turbulence generation and turbulent material mixing seeking to better match the fully 3D simulation data. For the first method, we enhanced the initial interface roughness by factors of $\chi = 1,10,100$ in the context of pure 2D-3D data rotation, but found that this did not improve our results by any of the metrics considered. For the second

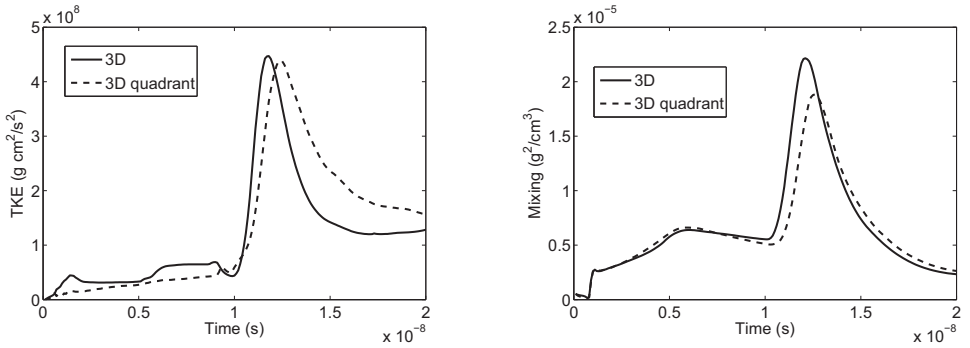

FIG. 8. Integrated flow quantities for the reshock simulations.

method, we perturbed the 2D-3D rotation mapping used to initialize the state and velocity variables. We used the same perturbations as in the first method, enhanced by factors of $\chi = 1, 10, 30$, to also directly affect the 2D-3D mapping function. We found that good matches to the 3D data can be obtained with the latter strategy when using $\chi = 30$, corresponding to the RMI growth rate of the longest-wavelength mode up to the time of rotation. It is likely because the perturbation spectrum relevant to instability growth in the problem (see Fig. 2) peaks at the longest wavelengths. This is also the case in the ICF experiments we consider in the following (see Sec. III A). Nevertheless, for cases in which long-wavelength perturbations are not dominant, it remains an open question as to whether this method is adequate.

III. ICF SIMULATIONS

We perform simulations of the implosion of a simple ICF capsule with a polystyrene shell of width $d = 20$ μm and outer radius $r = 437.5$ μm filled with 0.27 μg of deuterium gas (see Fig. 9). This models a number of capsules which have been imploded at the University of Rochester's OMEGA laser facility. These capsules are driven by a direct-drive approach using all 60 beams of the OMEGA laser. In order to study the relative importance of drive asymmetry and surface defects to the degradation of yield, we perform simulations with both a uniform drive and with drive asymmetries modeling those observed when using the OMEGA laser [41]. In both cases, a total of 24 kJ is deposited directly into the outer polystyrene shell over a period of approximately 1.35 ns.

In what follows, we discuss surface roughness and drive asymmetries in Sec. III A. Next, in Sec. III B, we discuss the growth of hydrodynamic instabilities seeded by these sources of asymmetry. We use this to inform a 2D-3D perturbation strategy similar to that used in the reshock simulations, which is described in detail in Sec. III C. Results of simulations using our 2D-3D strategy are discussed and compared to standard 2D-3D strategies, reduced-dimension simulations, and experimental data in Sec. III D.

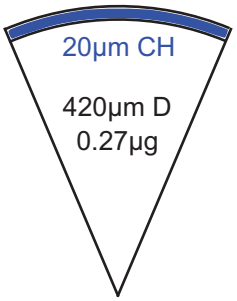

FIG. 9. (Color online) Diagram of the ICF capsule.

A. Initial material interface conditions and drive asymmetries

Interface perturbations are applied initially on the inner and outer surfaces of the polystyrene shell. The interface perturbations are applied radially as a sum of spherical harmonics:

$$\zeta(\theta,\phi) = \chi\Gamma \sum_{l=1}^{5} \sum_{\substack{-l \leqslant m \leqslant l \\ \sqrt{l^2+m^2} \leqslant 5}} a_{l,m} e^{im\phi} P_l^m[\cos(\theta)], \quad (6)$$

where P_l^m is an associated Legendre polynomial, $\{a_{l,m}\}$ are set so the perturbations have the outer surface spectrum in Fig. 10 (defined in Ref. [9]), and Γ is set so that the standard deviation of the perturbations is 1 μm. Note that we only include modes with $l \leqslant 5$ due to the sharp drop in the perturbation spectrum beginning at $l \approx 5$. The constant $\chi = 1$

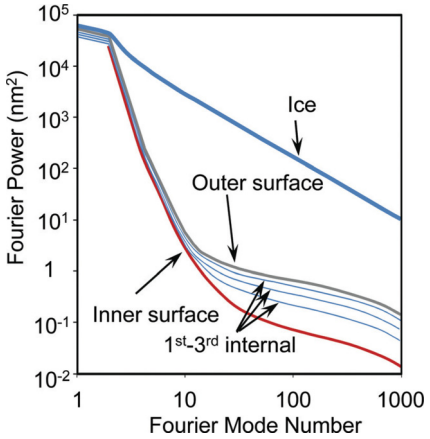

FIG. 10. (Color online) Approximate surface roughness power spectra for the various surfaces in an ICF capsule, obtained from [9].

for interface perturbations and $\chi = 10,20$ for 2D-3D mapping perturbations, discussed in the following.

We model the drive asymmetries in the implosion on work done by Marshall *et al.* [41] profiling the drive of the OMEGA laser. Specifically, we apply a P_{30} perturbation with 1.2% standard deviation to the ablator layer where energy is deposited to model the drive at $t = 0$. We do not model beam imbalances in the present simulations. However, the spectrum of beam imbalances is similar to that of surface defects [11], so some of the effects of long-wavelength asymmetries that we attribute to surface defects may be caused by beam imbalances in experiment.

B. Hydrodynamic instability growth in an ICF capsule

The dominant hydrodynamic instability during an ICF implosion is the Rayleigh-Taylor instability (RTI), which occurs at early times as ablator material accelerates into the surrounding gas and at "stagnation," when the shell decelerates due to increased fuel pressure. The fuel-ablator interface is also subject to the RMI as the shock exits the shell at early times and at later times when reflected shocks interact with the interface between the shell and the fuel. In addition, perturbations grow due to Bell-Plesset effects (see, e.g., [4]), in which incompressible fluid perturbations grow in a converging geometry as a consequence of mass conservation.

For the classical RTI in planar geometries, perturbations with wave number k grow exponentially [42] as $a(t) = a_0 \exp(\sqrt{Agk}t)$, where $A = \frac{\rho_0 - \rho_l}{\rho_0 + \rho_l}$ is the Atwood number and g is the acceleration. In a converging spherical geometry, this equation must be modified to include Bell-Plesset convergence effects, whose growth is coupled to the RTI growth [4], yielding

$$a(t) = a_0 \exp\left(\int_0^t \gamma_0(s)\, ds \right), \tag{7}$$

where

$$\gamma_0^2(t) = \frac{l(l+1)}{R} \frac{\rho_0 - \rho_1}{l\rho_0 + (l+1)\rho_1} g. \tag{8}$$

Here, l is the Legendre mode number, and R, ρ_0, ρ_1, and g are time-dependent quantities. Aided by 2D calculations, we can estimate, taking the maximum over the dominant modes $1 \leqslant l \leqslant 5$,

$$\chi = \frac{a(1.4\text{ ns})}{a_0} \approx 15.$$

Shorter-wavelength modes are neglected due to their vanishingly small amplitudes, as seen in Fig. 10.

The above estimate neglects feedthrough effects from the ablative RTI, RMI effects, mode coupling, and the spatial nonuniformity of instability growth in an ICF implosion. Without purely 3D data to compare to, there is significant uncertainty in the estimate. Therefore, we perform simulations using $\chi = 10$ and 20 in order to obtain approximate upper and lower bounds on instability growth rates for the long-wavelength modes and their effects on capsule performance.

C. 2D-3D mapping for ICF capsule simulations

For our ICF capsule simulations, 2D-3D mapping is performed at 1.4 ns. This is the approximate time at which the shock wave converges at $r = 0$. The unperturbed mapping is the same as for the reshock problem, namely, all state and velocity variables were set using the mapping

$$\begin{Bmatrix} x \\ y \end{Bmatrix} = \begin{Bmatrix} \sqrt{x'^2 + z'^2} \\ y' \end{Bmatrix},$$

where (x,y) are the coordinates for the 2D problem and (x',y',z') are the coordinates for the 3D problem. Vector-valued quantities, such as the velocity, were also appropriately rotated.

We performed simulations where the 2D-3D map was perturbed using the perturbation function $\zeta(x,z)$ defined in Eq. (6) using $\chi = 10$ and 20 to obtain upper and lower bounds on perturbation growth for comparison with experimental results. Specifically, the perturbed mapping was defined as

$$\begin{Bmatrix} x \\ y \end{Bmatrix} = \begin{Bmatrix} r' + \zeta\left[\arctan\left(\frac{z'}{x'}\right), \arctan\left(\frac{y'}{r'}\right)\right] \\ y' \end{Bmatrix},$$

where $r' := \sqrt{x'^2 + z'^2}$.

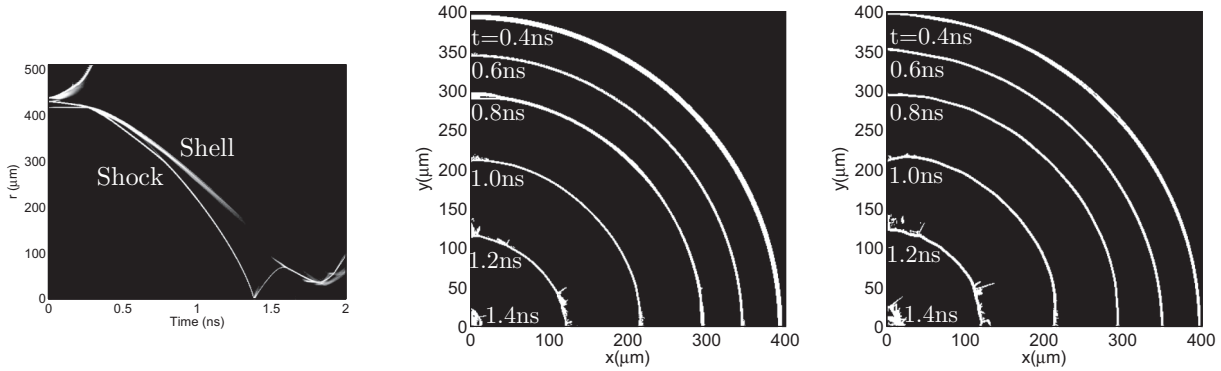

(a) 1D (b) 2D with no drive asymmetry (c) 2D with drive asymmetry

FIG. 11. (a) Shock and shell position versus time from a 1D calculation. (b), (c) Shock profiles in 0.2-ns increments from 0.4 to 1.4 ns (time of rotation) for 2D phase without (b) and with (c) drive asymmetry.

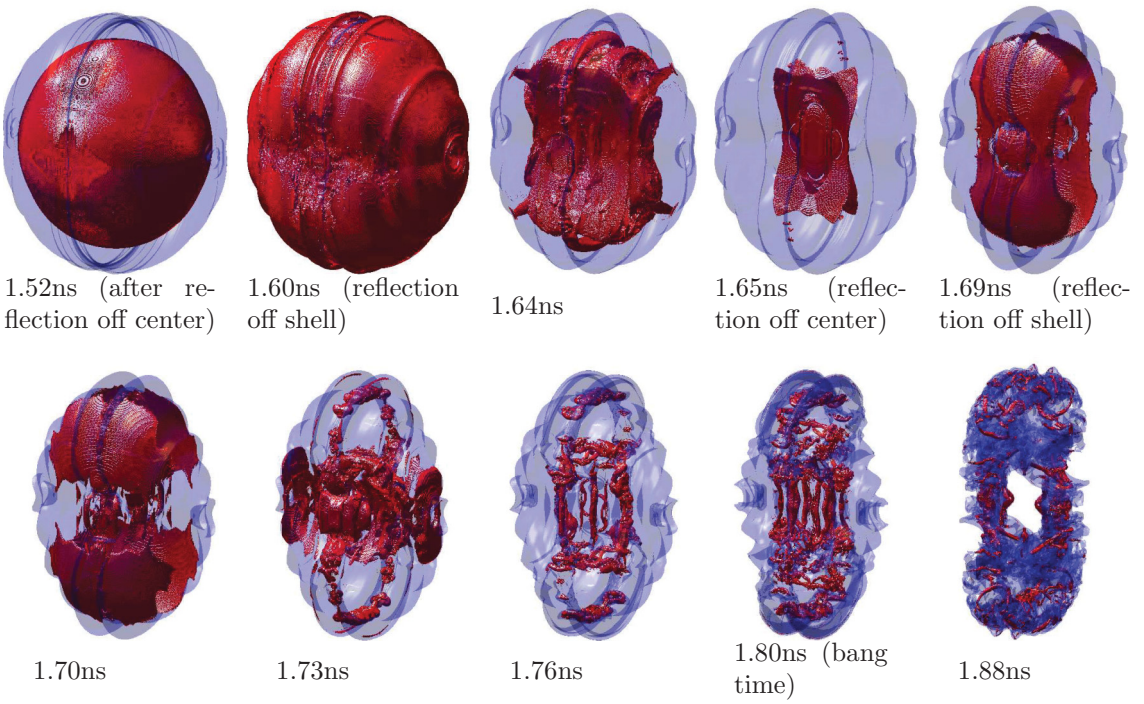

FIG. 12. (Color online) Visualization of the main shock (in red) and its interactions with the interface between the shell and the fuel (in blue) for the 3D phase of the 1/8-μm resolution 2D-3D simulation with no drive asymmetry and $\chi = 10$. In order to maximize displayed detail for a converging problem, these pictures do not show the same spatial extent.

D. Results

In Fig. 11(a), we show the shock and shell position versus time from a 1D calculation. This shows the shock colliding with itself at the center of the capsule at 1.4 ns proceeded by a series of reflections off the interface between the shell and the fuel and the center. In Figs. 11(b) and 11(c), we show shock profiles from the 2D phase of our 2D-3D simulations without and with drive asymmetry, respectively. This covers the period of the implosion from 0.4–1.4 ns as the shock is converging for the first time.

In Fig. 12, we show visualizations of the main shock as it traverses the gas from 1.52 through 1.88 ns for the 3D phase of the 1/8-μm resolution 2D-3D simulation with no drive asymmetry and $\chi = 10$. During this period, having reflected off the center at approximately 1.40 ns, the main shock reflects off the shell at approximately 1.60 ns. This interaction distorts the shock shape significantly due to the deformed shell shape. As the shock converges again at approximately 1.65 ns, it does not converge to a point due to its distorted shape; rather, the shock becomes oblate then breaks in two as it reflects off the center again. When these two resulting shocks proceed to interact with the now highly distorted shell at approximately 1.69 ns, they break apart further into many smaller shocks traveling in all directions. Each time a shock interacts with shell material, it induces a Richtmyer-Meshkov instability, which leads to turbulent mixing of gas and shell material.

The evolution of the main shock as it traverses the gas is largely the same for the simulations with drive asymmetry, although the shock breaks up faster due to the presence of shorter-wavelength (P_{30}) deformations of the shell. In Fig. 13,

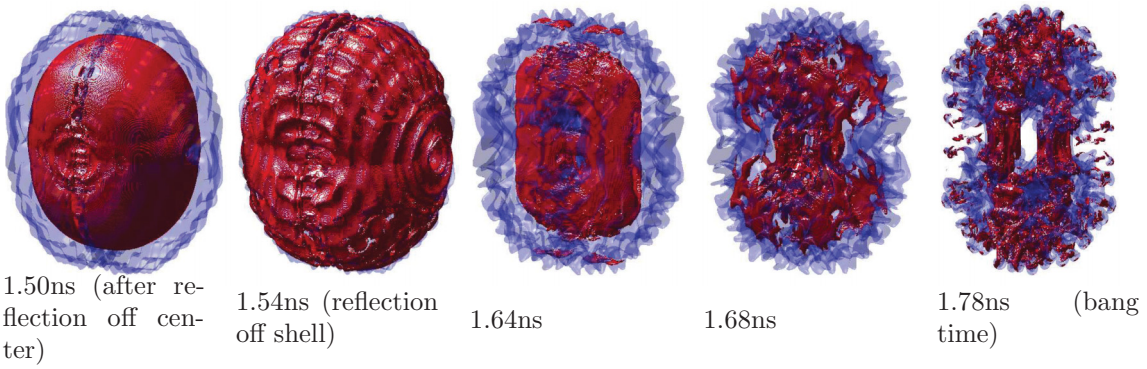

FIG. 13. (Color online) Visualization of the main shock (in red) and its interactions with the interface between the shell and the fuel (in blue) for the 3D phase of the 1/2-μm resolution 2D-3D simulation with drive asymmetry and $\chi = 20$. In order to maximize displayed detail for a converging problem, these pictures do not show the same spatial extent.

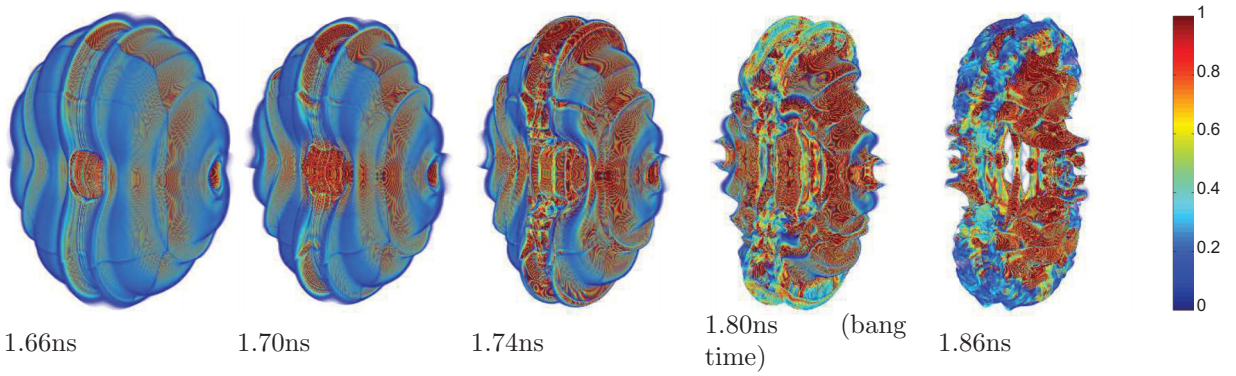

FIG. 14. (Color online) Visualization of the deuterium mass concentration for the 1/8-μm resolution simulation with $\chi = 10$ and no drive asymmetry. In order to maximize displayed detail for a converging problem, these pictures do not show the same spatial extent.

we show visualizations of the main shock as it reflects inside the gas from 1.50 through 1.72 ns for the 3D phase of the 1/2-μm resolution 2D-3D simulation with drive asymmetry and $\chi = 20$. During this period, having reflected off the center at approximately 1.40 ns, the main shock reflects off the shell at approximately 1.54 ns. This distorts the shock shape significantly due to the deformed shell shape. As the shock converges once more, it breaks up into many smaller shocks as the shock interacts with itself and protruding pieces of shell, and it is no longer possible to distinguish a main shock.

In Fig. 14, we show a visualization of the deuterium mass concentration for the 1/8-μm resolution simulation. Long-wavelength surface defects seed vortex rings that pull shell material into the gas and fragment it. Significant mixing develops near the interface between the shell and the fuel at bang time and quenches the burn as shell material protrudes through the center of the gas, even as the gas retains an overall shape that is fairly spherical. While no imaging was performed for relevant OMEGA experiments, ICF experiments at the National Ignition Facility are typically oblate [18] and have been observed to develop a similar toroidal shape near bang time [43].

The somewhat "squarish" shape of the gas in Fig. 14 reflects the directional splitting strategy used by the Riemann solver in the RAGE code. Nevertheless, the shape-distorting effects of this feature are dominated by the instability growth due to long-wavelength surface defects. Therefore, the negative effects are largely cosmetic and do not have a significant impact on the quantitative results presented below.

In Fig. 15, we show a visualization of the hot-spot shape, defined as the $T_{\text{ion}} = 1$ keV isosurface. It is notable that small-scale features are not present until approximately 1.85 ns, after bang time. This visualization more clearly shows the hole that develops in the center of the hot spot that quenches the burn, while the hot spot maintains a fairly spherical shape until after bang time.

E. Capsule performance and comparison to experiment

Many thermonuclear reactions take place in the capsule during its implosion. We focus our attention on the $D + D \rightarrow n + He^3$ reaction, for which experimental data are available for comparison. While experimental data about the $D + T \rightarrow n + \alpha$ reaction are also available, we can not accurately simulate this reaction with the Singe package since it relies on the presence of T produced by the $D + D \rightarrow p + T$ reaction, whose products are deposited locally. In experiment, the majority of these reactions take place after the tritons, generated with energies of 1 MeV, have slowed down to $\approx$50 keV, where the $D+T \rightarrow n+\alpha$ reaction rate peaks. By the time this has occurred, the tritons have traveled a sufficient distance to invalidate the assumption of local deposition. For this reason, the number of neutrons produced by this

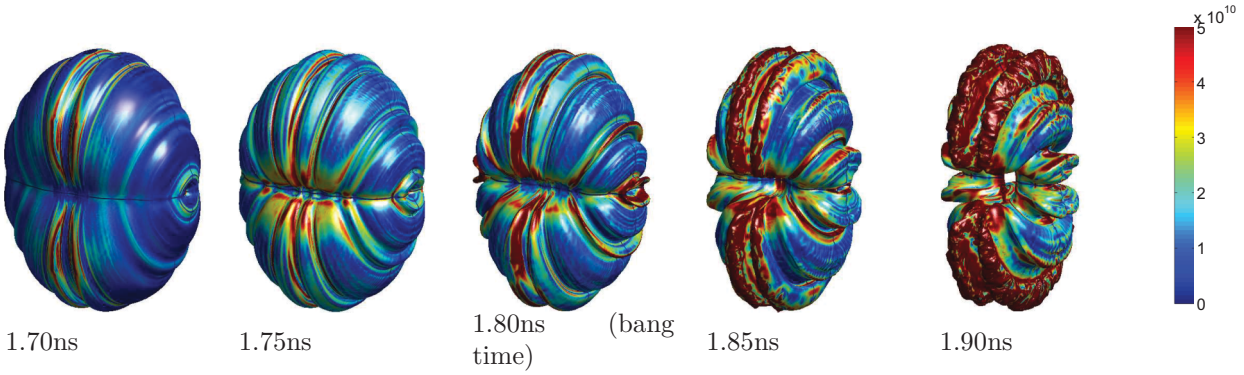

FIG. 15. (Color online) Visualization of hot-spot shape, defined as the $T_{\text{ion}} = 1$ keV isosurface, colored with vorticity magnitude (in s^{-1}) for the 1/8-μm resolution simulation with $\chi = 10$ and no drive asymmetry. In order to maximize displayed detail for a converging problem, these pictures do not show the same spatial extent.

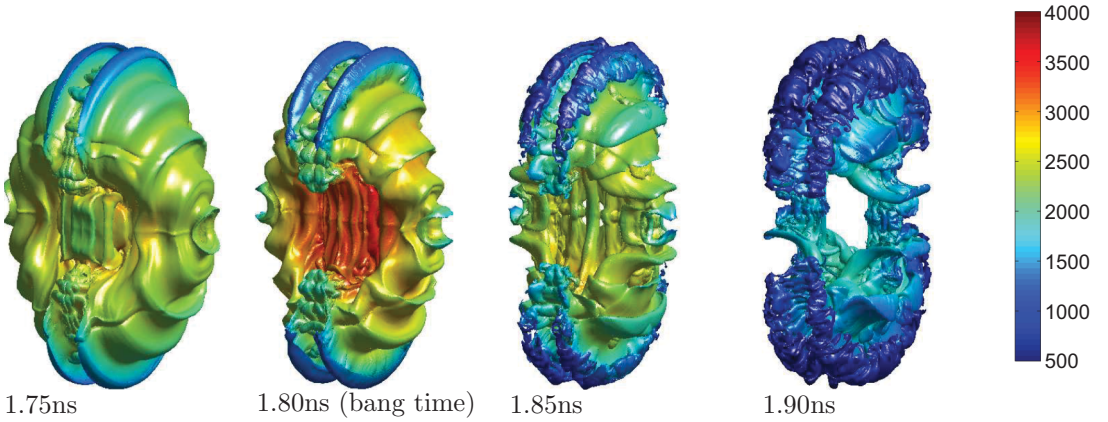

FIG. 16. (Color online) Deuterium mass concentration $c_D = 0.1$ isosurface colored with T_{ion} (in eV) calculated from the $1/8$-μm simulation data with $\chi = 10$ and no drive asymmetry. In order to maximize displayed detail for a converging problem, these pictures do not show the same spatial extent.

reaction is significantly underpredicted, and so we do not report these results. In the absence of any data about how deuterium and shell material are distributed at a sub-grid scale, we perform calculations in two limiting cases: "clean," in which the deuterium is assumed to burn in "chunk" form (i.e., it is atomically isolated from the shell material), and atomically mixed, in which the shell material in a cell is assumed to be uniformly atomically mixed with the deuterium.

In Fig. 16, we show a deuterium mass concentration $c_D = 0.1$ isosurface colored with the ion temperature T_{ion} (in eV) for the $1/8$-μm resolution simulation data. This gives an indication of the approximate fuel and shell interfaces and the temperature there. The annular region that contains most of the fuel mass has a lower temperature than the thin fuel region in the center, where the burn rates are highest. It is notable that the hot spot, defined as the region where $T_{ion} \geqslant 1$ keV, extends beyond this surface and contains part of the shell.

Results are presented in Table I for $1/2$-μm resolution simulation data. For the 2D-3D simulations, data are averaged over two simulations, with $\chi = 10,20$, and using two techniques for performing neutron production rate calculations: "clean" and atomically mixed, as defined above. For the other simulations, data are averaged over the two neutron production rate calculations. Presented uncertainties are the standard deviations. Here, we show the yield in terms of the total number of neutrons produced by the $D + D \rightarrow n + He^3$ reaction, as well as bang time (the time at which the DD neutron production rate reaches its peak), the burn-weighted ion temperature, and the burn width (the temporal extent of the burn, calculated as the time during which the neutron production rate exceeds half of its maximum). For the atomically mixed calculations, the DD neutron yield was typically ≈15% lower and the ion temperatures ≈3% higher than for the "clean" calculations. For comparison, we show results from a 2D simulation and a 2D-3D simulation with no mapping perturbations. Comparing 2D-3D results with mapping perturbations, we see that a majority of yield degradation results from long-wavelength surface defects. It is notable that drive asymmetry extends the burn width. This is due to the fact that the perturbations associated with drive asymmetry lead to the presence of several burn regions that are separated both spatially and temporally.

In order to perform a comparison to experimental data, we performed a $1/2$-μm simulation adapted to OMEGA shot 65036 [44]. This shot differs from the capsule considered above by the inclusion of a 1.8% titanium dopant in a 2-μm-wide layer adjacent to the fuel. While this dopant does not affect the hydrodynamic development of the capsule appreciably, it raises the ion temperature in the fuel by absorbing some of the energy radiated by the hot spot and changing the heat conductivity of the doped portion of the shell. In Table II, we show a comparison of our simulation of shot 65036 to available experimental data from [44]. The simulation uses a growth factor of $\chi = 10$ for the perturbations in the 2D to 3D mapping and neutron production rates are calculated in the "clean" limit. The comparisons to all available experimental data are well within the experimental uncertainties. We are unaware of any previous simulations that

TABLE I. Integrated quantities for $1/2$-μm ICF capsule simulations. For the 2D-3D simulations with mapping perturbations, data are averaged over four simulations, with $\chi = 10,20$ and using two techniques for performing neutron production rate calculations: "clean" and atomically mixed. For the other simulations, data are averaged over the two neutron production rate calculations.

	DD neutron yield (10^{10} neutrons)	Bang time (ns)	Burn weighted T_{ion} (KeV)	Burn width (ns)
2D	36.1 ± 4.9	1.79 ± .01	3.2 ± .3	0.11 ± .01
2D-3D with no mapping perturbations and no drive asymmetry	28.7 ± 2.9	1.74 ± .02	3.4 ± .1	0.09 ± .02
2D-3D with surface defects	14.6 ± 3.6	1.75 ± .01	2.8 ± .2	0.11 ± .01
2D-3D with surface defects and drive asymmetry	9.7 ± 2.6	1.78 ± .01	2.7 ± .2	0.15 ± .02

TABLE II. Comparison to experiment (OMEGA shot 65036 [44]) for 1/2-μm ICF capsule simulation. The simulation uses a growth factor $\chi = 10$, neutron production rates are calculated in the "clean" limit, and a titanium dopant was added to the shell as in experiment.

	DD neutron yield (10^{10} neutrons)	Bang time (ns)	Burn weighted T_{ion} (KeV)	Burn width (ns)
Experiment	$3.39 \pm .09$	$1.71 \pm .03$	$3.7 \pm .5$	$0.15 \pm .03$
Simulation	3.33	1.72	3.7	0.13

TABLE III. Integrated quantities as a function of grid resolution for 2D-3D ICF simulations with no drive asymmetry and $\chi = 10$. Neutron production rates are calculated using the "clean" method.

Simulation resolution	DD neutron yield (10^{10} neutrons)	Bang time (ns)	Burn weighted T_{ion} (KeV)	Burn width (ns)
1/2 μm	19.0	1.74	3.0	0.10
1/4 μm	23.4	1.74	3.2	0.09
1/8 μm	15.4	1.80	3.0	0.09

have been able to match the neutron yield, bang time, burn width, and burn-weighted ion temperatures from experiment simultaneously without tuning.

Grid resolution studies for integrated quantities are given in Table III. While the bang time, burn-weighted ion temperature, and burn width do not show appreciable variation, the neutron yield varies by approximately 20%. This is a reflection of how sensitive the reaction rate is to the distribution of gas and shell material, which is in turn highly sensitive to resolution and initial conditions in imploding problems.

IV. CONCLUSIONS

We have presented an improved strategy for performing simulations that begin in 2D and are later rotated to 3D. This strategy compensates for the reduced turbulence development in the 2D phase of the simulation as well as the artificial smoothing effects of the 2D-3D rotation, and was validated using simulations of a laser-driven reshock problem for which previously reported fully 3D simulation data are available. We applied our method to simulate the implosion of a simple OMEGA-type ICF capsule, consisting of a polystyrene shell surrounding deuterium gas.

Our ICF simulations compared well with available experimental data. We demonstrated that the dominant mechanism for yield degradation in the capsule compared to lower-dimensional simulations is the displacement of fuel from the hot spot by shell material induced by turbulent instability growth generated by long-wavelength surface defects. In our simulations, this resulted in yield degradation of approximately 60%. This effect is compounded by drive asymmetry, which breaks up the burn region both spatially and temporally, reducing the yield in our simulations by a further 30% and extending the burn width by approximately 40%. Thus, discrepancies between the yield predicted by previous simulations of ICF implosions can be explained by the reduced growth of turbulent instabilities inherent in reduced-dimension hydrodynamic simulations and the absence of appropriate modeling of long-wavelength asymmetries that are present due to surface defects and drive asymmetries.

ACKNOWLEDGMENTS

The authors would like to thank M. Daniels and M. McKay for code debugging assistance as well as L. Welser-Sherrill for useful discussions. The authors would also like to thank P. Bradley for assistance in modeling OMEGA shot 65036. Los Alamos National Laboratory is operated by Los Alamos National Security, LLC for the US Department of Energy NNSA under Contract No. DE-AC52-06NA25396.

[1] J. Nuckolls, L. Wood, A. Thiessen, and G. Zimmerman, Nature (London) **239**, 139 (1972).
[2] B. M. Haines, F. F. Grinstein, and J. D. Schwarzkopf, J. Turbulence **14**, 46 (2013).
[3] V. A. Thomas and R. J. Kares, Phys. Rev. Lett. **109**, 075004 (2012).
[4] R. Epstein, Phys. Plasmas **11**, 5114 (2004).
[5] B. M. Haines, F. F. Grinstein, L. Welser-Sherrill, and J. Fincke, Phys. Plasmas **20**, 022309 (2013).
[6] S. W. Haan *et al.*, Phys. Plasmas **2**, 2480 (1995).
[7] D. A. Callahan *et al.*, J. Phys. Conf. Ser. **112**, 022021 (2008).
[8] D. S. Clark, S. W. Haan, B. A. Hammel, J. D. Salmonson, D. A. Callahan, and R. P. J. Town, Phys. Plasmas **17**, 052703 (2010).
[9] S. W. Haan *et al.*, Phys. Plasmas **18**, 051001 (2011).
[10] P. B. Radha *et al.*, Phys. Plasmas **12**, 032702 (2005).
[11] P. B. Radha *et al.*, Phys. Plasmas **12**, 056307 (2005).
[12] P. B. Radha *et al.*, Phys. Plasmas **18**, 012705 (2011).
[13] K. Molvig, N. M. Hoffman, B. J. Albright, E. M. Nelson, and R. B. Webster, Phys. Rev. Lett. **109**, 095001 (2012).
[14] P. Amendt, O. L. Landen, H. F. Robey, C. K. Li, and R. D. Petrasso, Phys. Rev. Lett. **105**, 115005 (2010).
[15] E. S. Dodd *et al.*, Phys. Plasmas **19**, 042703 (2012).
[16] R. H. H. Scott, D. S. Clark, D. K. Bradley, D. A. Callahan, M. J. Edwards, S. W. Haan, O. S. Jones, B. K. Spears, M. M. Marinak, R. P. J. Town, P. A. Norreys, and L. J. Suter, Phys. Rev. Lett. **110**, 075001 (2013).
[17] D. S. Clark *et al.*, Phys. Plasmas **18**, 082701 (2011).
[18] G. P. Grim *et al.*, Phys. Plasmas **20**, 056320 (2013).
[19] P. Sagaut, *Large Eddy Simulation for Incompressible Flows*, 3rd ed. (Springer, New York, 2006).
[20] *Implicit Large Eddy Simulation: Computing Turbulent Flow Dynamics*, edited by F. F. Grinstein, L. G. Margolin, and W. J. Rider (Cambridge University Press, New York, 2010).
[21] L. Welser-Sherrill, J. Fincke, F. Doss, E. Loomis, K. Flippo, D. Offermann, P. Keiter, B. M. Haines, and F. F. Grinstein, High Energy Dens. Phys. J. **9**, 496 (2013).
[22] M. Gittings *et al.*, Comput. Sci. Discovery **1**, 015005 (2008).

[23] S. P. Lyon and J. D. Johnson, Los Alamos National Laboratory Report No. LA-UR-92-3407, 1992 (unpublished).
[24] C. C. Joggerst *et al.*, Los Alamos National Laboratory Report No. LA-UR-12-26671, 2012 (unpublished).
[25] B. M. Haines, F. F. Grinstein, L. Welser–Sherrill, J. R. Fincke, and F. W. Doss, Phys. Plasmas **20**, 092301 (2013).
[26] B. M. Haines, F. F. Grinstein, L. Welser–Sherrill, J. R. Fincke, and F. W. Doss, Phys. Plasmas **20**, 072306 (2013).
[27] W. K. George, in *Advances in Turbulence*, edited by W. K. George and R. E. A. Arndt (Springer, New York, 1989).
[28] W. K. George and L. Davidson, AIAA J. **42**, 438 (2004).
[29] G. Dimonte, Phys. Plasmas **6**, 2009 (1999).
[30] D. Youngs, in *Implicit Large Eddy Simulation: Computing Turbulent Flow Dynamics*, edited by F. F. Grinstein, L. G. Margolin, and W. J. Rider (Cambridge University Press, Cambridge, UK, 2010), Chap. 13.
[31] A. A. Gowardhan and F. F. Grinstein, J. Turbulence **12**, N43 (2011).
[32] R. D. Richtmyer, Commun. Pure Appl. Math. **13**, 297 (1960).
[33] Richard L. Holmes *et al.*, J. Fluid Mech. **389**, 55 (1999).
[34] F. F. Grinstein, A. A.-Gowardhan, and A. J. Wachtor, Phys. Fluids **23**, 034106 (2011).
[35] A. A. Gowardhan, J. R. Ristorcelli, and F. F. Grinstein, Phys. Fluids **23**, 071701 (2011).
[36] J. R. Ristorcelli, A. A. Gowardhan, and F. F. Grinstein, Phys. Fluids **25**, 044106 (2013).
[37] J. Jiménez, A. A. Wray, P. G. Saffman, and R. S. Rogallo, J. Fluid Mech. **255**, 65 (1993).
[38] Y. Zhou, F. F. Grinstein, A. J. Wachtor, and B. M. Haines, Phys. Rev. E **89**, 013303 (2014).
[39] P. E. Dimotakis, J. Fluid Mech. **409**, 69 (2000).
[40] Y. Zhou, Phys. Plasmas **14**, 082701 (2007).
[41] F. J. Marshall *et al.*, Phys. Plasmas **11**, 251 (2004).
[42] P. G. Drazin, *Introduction to Hydrodynamic Stability* (Cambridge University Press, Cambridge, UK, 2002).
[43] H. S. Park *et al.*, Phys. Rev. Lett. **112**, 055001 (2014).
[44] J. A. Baumgaertel *et al.* (unpublished).